

Segmented Mirror Coarse Phasing with a Dispersed Fringe Sensor: Experiment on NGST's Wavefront Control Testbed

Fang Shi^a, Dave C. Redding^a, Andrew E. Lowman^a, Charles W. Bowers^b, Laura A. Burns^c,
Peter Petrone III^d, Catherine M. Ohara^a, and Scott A. Basinger^a

^aJet Propulsion Laboratory, California Institute of Technology, Pasadena, CA 91109

^bGoddard Space Flight Center, NASA, Greenbelt, MD 20771

^cScience Systems and Applications Inc., Lanham, MD 20706

^dManTech Systems Engineering Corporation, Greenbelt, MD 20771

ABSTRACT

A piston sensing and control algorithm for segmented mirror coarse phasing using a dispersed fringe sensor (DFS) has been developed for the Next Generation Space Telescope (NGST) wavefront sensing and control. The DFS can detect residual piston errors as large as the order of a depth-of-focus and can phase the segment mirrors with accuracy better than 0.1 microns, which is well within the capture range of fine phasing for NGST. A series of experiments have been carried out on the NGST's Wavefront Control Testbed (WCT) to validate the modeling results, evaluate the DFS performance, and systematically explore the factors that affect the DFS performance. This paper reports the testbed results for several critical issues of DFS performance, including DFS dynamic range, accuracy, fringe visibility, and the effects of segment mirror aberrations.

Keywords: Space telescope, segmented mirror, wavefront sensing and control, dispersed fringe sensor

1. INTRODUCTION

Segmented mirror coarse phasing is part of the Next Generation Space Telescope (NGST) wavefront sensing and control (WFS&C) process during the early stages of NGST commissioning^[1]. It begins after the segmented mirrors are coarse aligned, a process that includes initial capture, tip-tilt alignment, and focusing of each segmented mirror. After coarse alignment, the segmented mirrors are aligned with residual tilt errors less than a fraction of the point spread function (PSF), and focused to within a depth-of-focus (DOF) of each segmented mirror. Although the residual tilts can be handled by the fine phasing, the residual piston errors (with amplitudes of ~ 1 DOF) are still many orders of magnitude larger than a wavelength and cannot be phased by the fine phasing algorithm^[2]. The dispersed fringe sensor (DFS) uses a transmissive grism as the dispersing element. It spreads the light according to its wavelength, forming a spectrum on the camera. Coherent addition of the wavefront error caused by piston variations between segments will result in the intensity modulation of the spectrum which is used by DFS algorithm to detect the wavefront piston errors. Coarse phasing with a dispersed fringe sensor (DFS) provides NGST the wavefront sensing and control of large relative piston errors among the NGST segmented primary mirrors. It reduces the piston errors to within the capture range of fine phasing, the last step in the wavefront sensing and control process^[1].

The DFS piston detection algorithms and processing software were developed using realistic optical models. The NGST's Wavefront Control Testbed (WCT) is used to develop candidate wavefront sensing and control algorithms proposed for use on NGST. With three segmented mirrors and two deformable mirrors, the WCT provides a flexible testing environment for segmented mirror wavefront sensing and control. Since our earlier DFS experiments on WCT using the transmissive phase plates^[3], our experiments on the testbed have been concentrated on the DFS piston detection with the segmented mirrors. Tests have been designed to understand the capabilities of DFS and to explore the performance of DFS under various influence factors. This paper will describe the principle of using a DFS to detect the

relative wavefront piston, report some of the key experiment results, discuss the limitations of the DFS, and describe the future plans of DFS testing and development.

2. DISPERSED FRINGE SENSOR FOR SEGMENTED MIRROR PISTON DETECTION

The dispersed fringe sensor uses a transmissive grism as the dispersing element. The grism disperses the light from a broadband source according to its wavelength, forming a spectrum on the camera. The wavelength dispersion relation along the dispersion direction x is

$$\lambda(x) = \lambda_0 + \frac{\partial \lambda}{\partial x} \cdot x = \lambda_0 + C_0 \cdot x \quad (1)$$

where λ_0 is the central wavelength and C_0 is the linear dispersion coefficient, which depends on the characteristics of the grism. Coherent addition of the wavefront error due to the relative piston of the segmented mirrors will result in the intensity modulation within the spectrum. The field intensity at any point $E(x)$ along the dispersion is the sum of the fields from the de-phased segments:

$$E(x) = E_1 e^{i[2\pi/\lambda(x)L]} + E_2 e^{i[2\pi/\lambda(x)(L+\delta L)]} \quad (2)$$

where E_1 and E_2 are the amplitude of the two segments ($E_1 = E_2$ when they come from two equal area segmented mirrors), L is the diffraction length, and δL is the wavefront optical path length difference due to the piston between the segments. Along the dispersed spectrum, the wavefront may add constructively or destructively, depending on local wavelength and global piston error. Periodic dark bands are formed within the PSF when λ is such that the destruction condition $(2\pi/\lambda) \cdot \delta L = \pi$ is met (see Figure 1). Along the dispersion direction the fringe intensity pattern has the form:

$$I(x, y) = I_0 \left[1 + \gamma \cdot \cos \left(2\pi \cdot \frac{\delta L}{\lambda(x)} + \phi_0(y) \right) \right] \quad (3)$$

where $I(x, y)$ is the DFS fringe intensity along the dispersion coordinate x , γ is the fringe visibility, and ϕ_0 is a phase constant that depends on where the DFS fringe is extracted. Generally, the intensity of the central row pixels along the dispersion is used as the main DFS signal. It is chosen because it has the highest intensity level. Eq. 3 has shown that the fringe modulation period is related to the piston error – a larger piston will cause more fringes. Figure 1 shows a DFS fringe image from WCT and the extracted DFS signals. The signals from rows above and below the main DFS signal row also have similar modulations except for a phase shift ($\phi_0(y)$) between adjacent rows of pixels. The relative phase shift between these two rows can be used to determine the sign of wavefront piston δL because the lag or lead of the phase shift depends on the sign of the wavefront piston. The DFS fringe analysis algorithm uses all three rows to determine the four parameters in the fringe equation of Eq. (3): I_0 , γ , ϕ_0 , and piston error δL using the least squares method. With knowledge of the piston value and sign, the testbed control software can control the segment mirrors' actuators to remove the piston error and phase the segmented mirrors. When the segmented mirrors are phased the wavefront is coherently added for the entire wavelength and the spectrum will not show any modulations. When the relative piston error is small, the DFS signal modulation becomes incomplete. A DFS signal with an incomplete modulation cycle over the spectrum may result in erroneous piston detection. However, the small wavefront error δL can still be reliably detected by adding a predetermined piston phase ΔL to the segment being tested so that total wavefront phase error from the piston $P = \Delta L + \delta L$ is large enough to form a DFS signal with some modulations so that DFS can accurately detect it.

The basic requirement for coarse phasing requires that the maximum detectable piston is at least 1 DOF (depth of focus is defined as $\text{DOF} = \pm 2\lambda F^2$, where λ is the wavelength and F is the F-number) of a segmented mirror, and it should bring the piston error down to within the detection range of fine phasing or the PSF monitoring process using the In-focus PSF Optimizer (IPO) [7]. To reliably detect the piston, the DFS fringe should be resolvable by the detector, which

is equivalent to having at least 4 PSFs per fringe cycle. The DFS fringe equation Eq. (3) has indicated that, for any given piston, the DFS fringe is the densest at the blue wavelength end, therefore, the blue end fringe resolution determines the maximum detectable wavefront piston. The DFS design is determined by the choice of four parameters: (1) the grism spectral resolution $R_0 = mD/d$, where m is the grating diffraction order, D is the telescope diameter, and d is the grating groove space projected on the sky; (2) the blue end wavelength λ_B ; (3) the critical sample wavelength λ_0 ; and (4) the DFS spectral detector window size N_{pixel} . It is convenient to relate the N_{pixel} with DFS dispersion R_0 , blue and red end wavelengths (λ_B and λ_R) as

$$N_{pixel} = 2R_0 \frac{\lambda_R - \lambda_B}{\lambda_0} \quad (4)$$

Then the relationship with the maximum wavefront piston error δL_{max} becomes

$$\delta L_{max} = \left[\frac{R_0}{4} \left(\frac{\lambda_B}{\lambda_0} \right) + 1 \right] \cdot \lambda_B \quad (5)$$

This requirement defines the grism dispersion power after the wavelength range is determined. When the wavefront piston is large, the blue end of the DFS spectrum may become under-sampled by the DFS. However, we can use only the partial spectrum at the red end where the fringe modulation is still resolved to detect and correct a larger wavefront piston error – a process we called the “DFS fringe windowing”. DFS fringe windowing will increase the maximum detectable wavefront piston and greatly increase the DFS dynamic range. However, DFS windowing reduces the number of pixels in the DFS signal which may lower the DFS’s signal-to-noise ratio.

3. DFS EXPERIMENTS ON WAVEFRONT CONTROL TESTBED

3.1 DFS Experiment on the Wavefront Control Testbed

The NGST’s WCT is a modular system which consists of (1) the Source Module which has a white light point source with both narrow and broad band filters, (2) the Simulator Module which can generate high-order aberrations using a 69-actuator deformable mirror (SMDM) and a wavefront piston using a set of transmissive phase plates^[3, 6], or contains three segmented mirrors that each can be accurately tilted and pistoned, (3) the Aft-Optics Module which contains a one-to-one imaging system, a 349-actuator deformable mirror (AODM), a fast steering mirror, a flip-in grism, and a CCD camera on a translation stage. The segmented mirrors in the WCT consist of three one-inch diameter spherical mirrors which are conjugate to the system aperture defined by the AODM. Each segmented mirror is driven by a PZT platform with 3 piezoelectric actuators which provide nanometer level control over a 12 μm range. The PZT platform is mounted on a kinematic mount actuated by picomotors. Compared to the full aperture of DM, the three segmented mirrors form a sparse aperture covering only about 30% of total aperture area formed by DM. The WCT is physically located at Goddard Space Flight Center and most of the experiments are run via the Internet from JPL by the WCT’s Segmented Telescope Control Software (STCS)^[5]. More detailed information of about the WCT hardware setup and capability can be found in references^[4, 6, 10, 11].

In WCT experiments the raw DFS signals contain some unwanted spectral features such as DFS grism spectral efficiency, wavelength dependence of detector quantum efficiency (QE) and spectra of the source (xenon arc-lamp for WCT testbed) which includes sharp emission and absorption lines. The dominant spectral features in the DFS fringe for WCT are the wavelength dependence of the CCD’s QE and source lamp emission lines. These unwanted spectral features should be removed before the DFS analysis so that the fringe contains only the modulations caused by the wavefront piston. For the WCT the unwanted spectral features are removed by dividing the raw DFS signals with a calibration spectrum. The so-called calibration spectrum is formed by summing the spectrum intensity across the DFS spectrum. Because modulations caused by the segment piston only appear within the PSF of a single segment, summing across the spectrum removes the spectrum information from the segment piston while leaving all other spectral features, which are only related to the wavelength, in the calibration spectrum. This signal preprocess results a clean DFS signal

spectrum governed by the relation in Eq. 3. Figure 1 demonstrates this DFS signal processing for the experimental data of WCT.

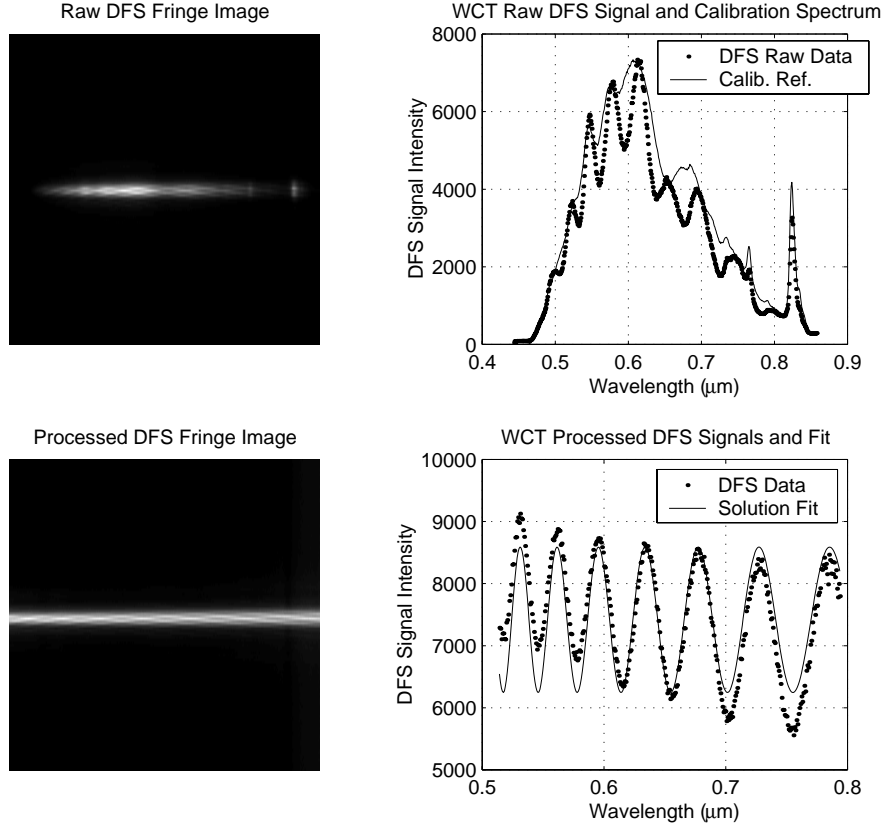


Figure 1. WCT DFS fringes and the process of removing the unwanted spectral features for WCT data. *Upper panels:* The raw DFS fringe image (*left*); plots of DFS signal (dots) and the calibration spectrum (line) (*right*). Notice how the DFS signal is buried within the broad spectrum with features that are dominated by the CCD quantum efficiency and sharp emission lines from the Xe arc lamp. *The Lower panels:* The fringe modulations are revealed in the DFS image (*left*) and signals (*right*) after the process has removed unwanted spectral features. Also on the lower right is the DFS piston solution fit for the detected piston.

3.2 DFS Segmented Mirror Piston Detection Accuracy

One of the important requirements for coarse phasing is DFS accuracy. DFS piston detection accuracy on WCT was studied by both modeling and experiment. The piston detection error \mathcal{E} is defined as the difference between the given piston P_{given} to the segmented mirror and the piston detected $P_{detected}$ by the DFS

$$\mathcal{E} = P_{given} - P_{detected} \quad (6)$$

Modeling on WCT has shown that the major contribution of DFS piston detection error comes from the uncertainty of the center row position at which the DFS signal is extracted. Furthermore, the fact that the WCT image was under-sampled for most of the spectrum made this effect worse. A multi-trace DFS method has been proposed to solve the problem of the uncertainty in DFS signal row positions. In the multi-trace DFS method, adjacent rows are also extracted as DFS signals as well as the main DFS signal. As in the single-trace method, for each signal an upper and lower row are also used to detect the piston sign. Two predetermined criteria based on the main signal intensity are used to select the signal rows and sign rows. These criteria guarantee that the DFS signals have a high enough signal-to-noise ratio.

Depending on the PSF size and CCD sampling, the multi-trace may contain three to seven rows of signals for WCT. The detected piston values from each multi-trace signal are weighted according to the solved I_0 and γ for their detection qualities, and the final piston $P_{detected}$ is derived from the average of all the valid piston detections. Multi-trace DFS can average out the uncertainty errors due to the near-linear relationship between the row positions and the detection errors. Figure 2 shows how multi-trace DFS works and gives an example from the WCT testbed results.

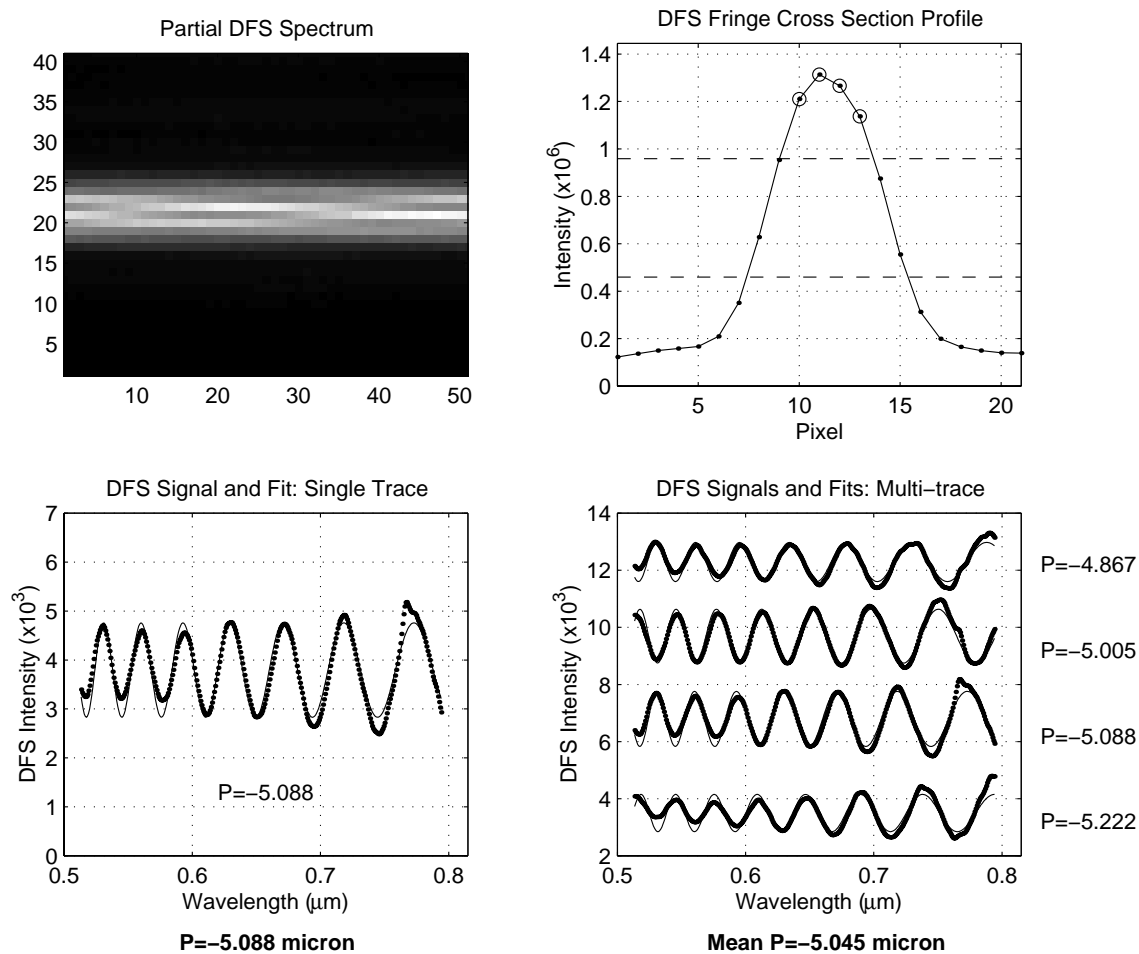


Figure 2. Single and multi-trace DFS. *Upper left:* a section of the DFS spectrum from WCT displayed in logarithmic scale. *Upper right:* accumulated cross section profile of the spectrum (connected dots). Circles indicate rows used for multi-trace signals. The upper horizontal dash line is the intensity criterion for selection of the signal row and the lower dash line is for the selection of the sign rows. Both criteria must be met for multi-trace DFS signals. *Lower left:* the single-trace DFS signal (dots) and its solution fit (line). *Lower right:* the multi-trace DFS signals from the same data and their fits. Intensity offsets are added to the traces to separate them in the plot. The fitted piston values show the systematic trend in the pistons detected against the signal row positions. The final piston values for both methods are shown at the bottom in bold font.

Modeling on WCT has shown that the multi-trace DFS method is very effective and can reduce the peak-to-valley (P-V) detection error from $\sim 0.3 \mu\text{m}$ to $\sim 0.07 \mu\text{m}$. Experimental tests were conducted to test DFS accuracy on the testbed. During the test, pistons of a segmented mirror were scanned through the PZT actuator range ($-6 \mu\text{m}$ to $+6 \mu\text{m}$) with a known step size. Segmented mirror actuator positions, read from the PZT controller, as well as DFS fringe images were recorded at each piston-scanning step. The single-trace and multi-trace DFS algorithms were then applied to detect the piston from the same DFS fringe images and the detected values were compared with the segment actuator positions. Each PZT actuator uses a strain gauge sensor to close the loop on its actuation position. This mechanism provides the PZT actuator with a sub-nanometer resolution, actuation linearity to 0.03% of the stroke, and a position repeatability

better than 5 nm [8]. This enabled us to use the PZT position read out to measure the DFS piston detection accuracy. To minimize the long term (~ 1 hour) drift of the testbed, the pistons between adjacent scan steps were compared, i.e., the piston detection error was defined as

$$\Delta P_i = |P_{\text{detected}}(i) - P_{\text{detected}}(i-1)| - |P_{\text{actuated}}(i) - P_{\text{actuated}}(i-1)| \quad (7)$$

where ΔP_i is the DFS measurement error at the i^{th} scanning step. Plots in Figure 3 summarize the results from the experiment on phasing segment #1 respect to reference segment #2 on WCT. The results show that the multi-trace DFS reduced the scattering of the piston detection errors, and hence increased the accuracy of the detection. The test data have shown that the multi-trace DFS reduced the DFS piston detection error by about a factor of 2, from piston detection error of 50 nm rms and $204 \text{ nm peak-to-valley}$ to detection error of 25 nm rms and $89 \text{ nm peak-to-valley}$.

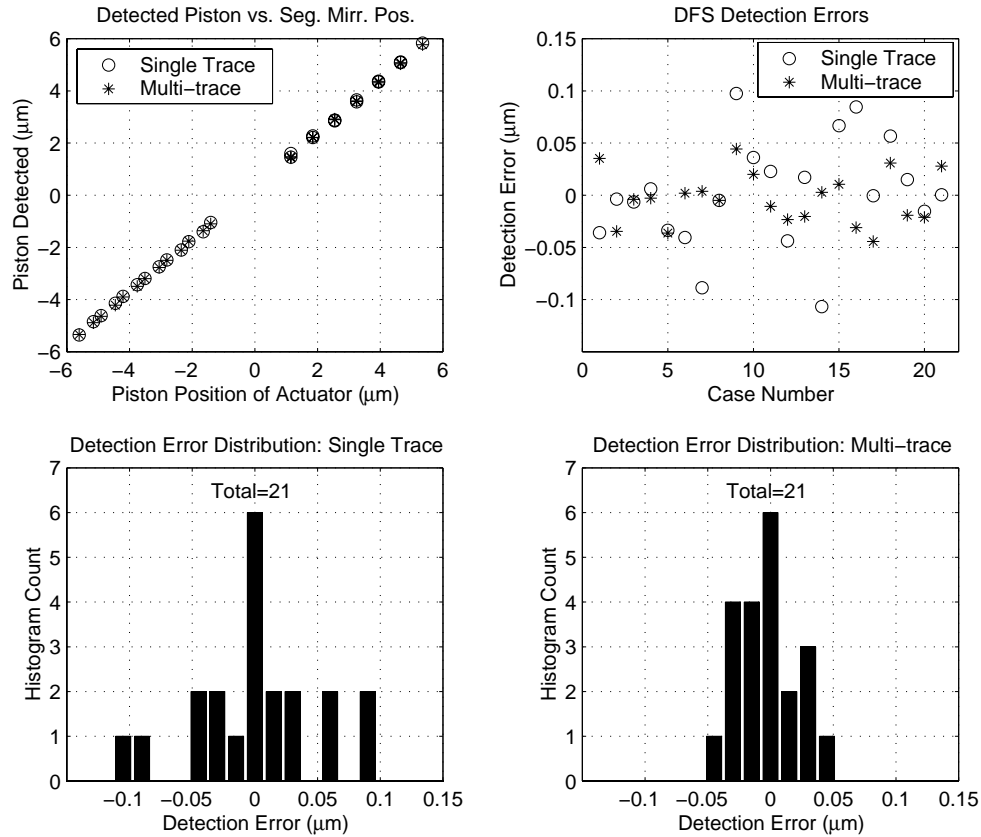


Fig. 3. DFS piston detection accuracy test results. *Upper left:* piston detected against piston position readout from the actuators. The group does not cross the zero due to the initial residual piston in the testbed. *Upper right:* piston detection error compared with adjacent piston scans as defined in Eq. 7. *Lower left:* the single-trace DFS piston detection error distribution. *Lower right:* the multi-trace DFS piston detection error distribution. There are total of 21 scan steps used in the plot. For single trace the piston detection error is 50 nm rms and $204 \text{ nm peak-to-valley}$ and for the multi-trace the detection error is 25 nm rms and $89 \text{ nm peak-to-valley}$.

3.3 DFS Piston Error Detection Dynamic Range

The limit of the DFS for detection of large wavefront pistons was tested and modeled on WCT. Because the PZT actuators of the segmented mirror in WCT can only provide a $12\text{-}\mu\text{m}$ stroke, we relied on the piezomotor stage in the segmented mirror assembly to generate large piston errors for the segments. Figure 4 shows the results from the modeling and experiment. The linearity and repeatability of the piezomotor stages is poor so its piston position readouts

are not reliable. However, we used the PZT actuators to add an accurate piston in addition to the large stroke piston generated by the picomotors as a check for the DFS performance. This is done by comparing the difference of the detected piston before and after the PZT piston with the value of PZT piston added. Since this study was designed to characterize the piston range in which the DFS can properly detect instead of the accuracy, we placed the piston positions according to the detection values with an estimated error bar of $\pm 3 \mu\text{m}$ on the picomotor position readout (piston given.) The plots indicate that for both the modeling and experiment, the DFS detection fails around 1 depth-of-focus for WCT. One of the factors that limit the DFS detection range is that the fringe from WCT is under-sampled for most of the spectral range. The results have also shown that using the partial DFS fringe at the red end of the spectrum can increase the detection range. The plots in Figure 4 have shown that the experiment and the modeling agree with each other on the DFS detection limit for large piston errors.

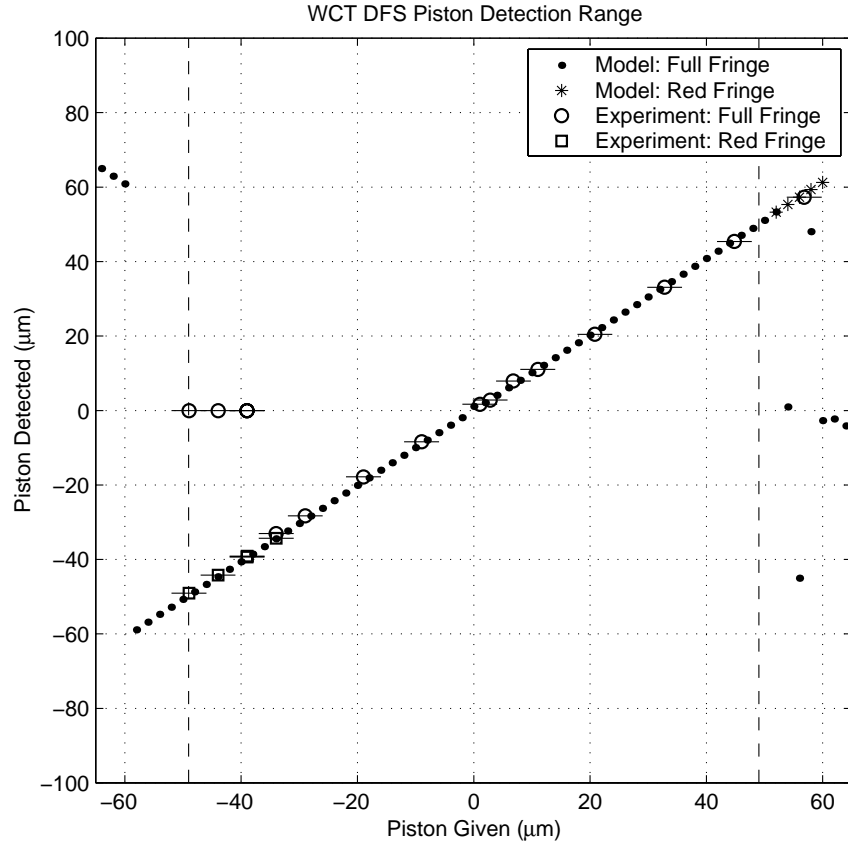


Figure 4. Results from DFS dynamic range tests from modeling and experiment on WCT. The plot shows the given piston versus the detected piston. DFS fringe windowing (“red fringe”) is applied when the detection from the “full fringe” has failed. An error bar of $\pm 3 \mu\text{m}$ is given to the picomotor piston readout. A pair of dashed lines indicates the range of the depth-of-focus.

3.4 DFS Fringe Visibility

One of the important characteristics of the DFS fringe is fringe visibility which measures the contrast of the modulation. The DFS detection accuracy depends on the fringe visibility because it determines the signal-to-noise ratio (SNR). The fringe visibility γ is defined as

$$\gamma = \frac{I_{\max} - I_{\min}}{I_{\text{mean}}} = 2 \times \frac{I_{\max} - I_{\min}}{I_{\max} + I_{\min}} \quad (8)$$

where I_{max} , I_{min} , and I_{mean} are the maximum, minimum, and mean DFS signal intensities, respectively. Modeling and experiments have shown that the DFS fringe visibility depends on the relative orientation between the DFS dispersion direction and the direction of the baseline that connects the two segmented mirrors. As described in section 2, the DFS fringe modulation is formed by the coherent addition of PSF intensities at each wavelength and the dispersive displacement of the PSF according to the wavelength. Depending on the relative orientation between the DFS dispersion direction and baseline, the side lobes of the combined PSF for each wavelength may fill inside the fringe and lower the visibility of the DFS fringe modulation. The highest DFS fringe visibility (contrast) occurs when the DFS disperses the light in the direction that is perpendicular to the baseline between the segments, the orientation at which the side lobes of all the wavelengths are parallel and separated from the main row of the DFS fringe.

Figure 5 shows the WCT experimental results for the relationship between fringe visibility and the angle between the dispersion and segment baseline. In this experiment, two segments were used and their relative piston was fixed as the grism was rotated at a step size of 5° . A DFS fringe image was taken at each grism orientation. The fringes were then analyzed and the fringe visibility was calculated from the solution fits. We used the fitted signal instead of the raw DFS signal for the fringe visibility calculation to minimize the influence of detector noise. The plots show that for WCT segmented mirrors the fringe visibility drops quickly to zero and remains at zero when the grism is about 30° away from the highest contrast position. The results also show that, in this test case in which Segment 2 was the reference segment, the visibility against the rotation curve is different when Segment 3 is pistoned up (positive piston) versus pistoned down (negative piston.) Again, we believe this can be explained with the argument from the way that PSF side lobes fill into the fringe.

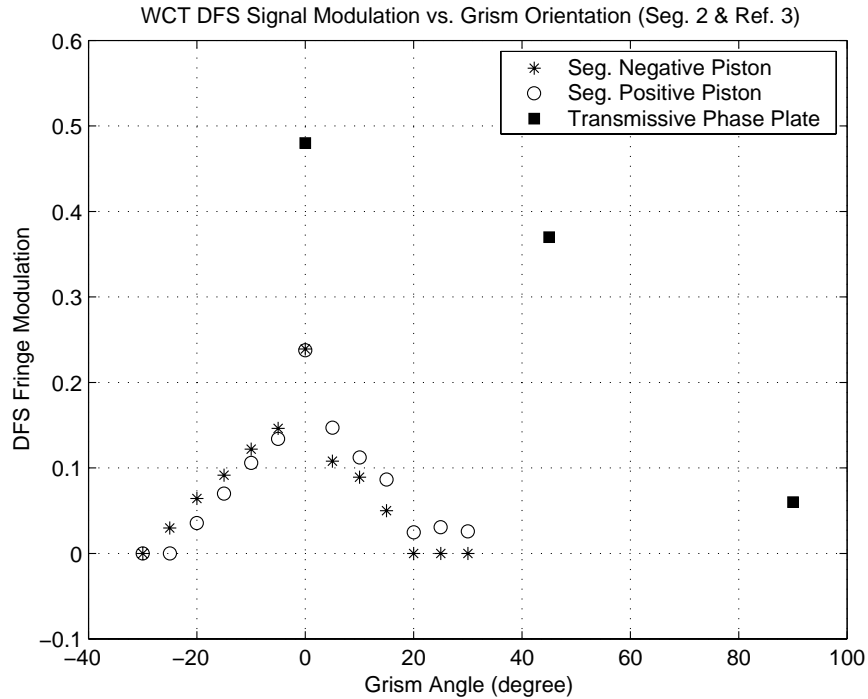


Figure 5. DFS fringe visibility of WCT segmented mirror against the rotation angle of the grism. 0° is the position at which the dispersion is perpendicular to the segments' baseline. The test was done for both positive piston (circles) and negative piston (asterisks.) The test has been done for the complete rotation of the grism. The plot only shows the grism angle range from -30° to $+30^\circ$. Beyond this angular range, the DFS visibility remains at zero. To demonstrate the effect of aperture sparseness we also plot the fringe visibility from our earlier experiments that used a transmissive plate which forms a full apertures (squares).

This orientation effect of the DFS fringe visibility also critically depends on the sparseness of the aperture formed by the segmented mirrors. For WCT, the segmented mirrors form a sparse aperture system; therefore its DFS fringe visibility has a stronger relation with the relative orientation of the grism. Figure 5 also plots the data obtained from our earlier experiment using a transmissive plate^[3]. Because the two piston halves of the transmissive plate form a full aperture, the visibility is still not totally washed out even at 90°.

3.5 Effect of the Segmented Mirror Surface Aberrations

Mirror aberrations include irregularities on the mirror surface and radius mismatch between the segmented mirrors. The wavefront degradation from the mirror surface aberrations results a larger PSF than that of a diffraction-limited PSF. The spreading of PSFs will lower the DFS signal's intensity as well as its fringe visibility, therefore lower the DFS signal-to-noise ratio and increase DFS piston detection error. Another effect of the mirror figure aberrations is that the aberrations may directly contribute to the error in the measured piston. This is because even if the mean wavefront piston over the segmented mirror is zero, the sub-region wavefront aberration may be picked up as the extra wavefront piston by the DFS, because the DFS signal is extracted from the sub-PSF region of the fringe. However, the multi-trace DFS algorithm described earlier can reduce this effect.

Tests have been conducted on WCT to explore the effect of segment aberrations on DFS performance. In the experiment, the AODM^[4] was used to add the wavefront aberration because the segments and AODM are conjugate to each other. Since the segmented mirrors form a sparse aperture compared with the AODM, the segments only see a portion of the added aberration. We need to take this into consideration when we calculate how much aberration is really added to the segments. We also need to take out the gross piston from the aberration seen by each segment. Figure 6 shows a typical result in which a $-1.0 \mu\text{m}$ Zernike coma was added to the AODM surface. The wavefront aberrations actually seen by the segments have a $P-V = 2.6 \mu\text{m}$ and rms $\sigma = 0.71 \mu\text{m}$. The PSF after the segments were realigned is shown in the figure. The plot on the right shows the obtained DFS signal and its solution fit. There is a $\Delta P = 0.17 \mu\text{m}$ detection error compared with the detection when AODM is flat. Our test on WCT is limited by the AODM deformation capability which, depending on the aberration modes, can only put up to about $\pm 1.2 \mu\text{m}$ of Zernike aberrations on the DM. Lower-order aberrations were tested, containing up to all third-order aberrations. The experiment has shown that DFS detection holds very well against wavefront aberrations.

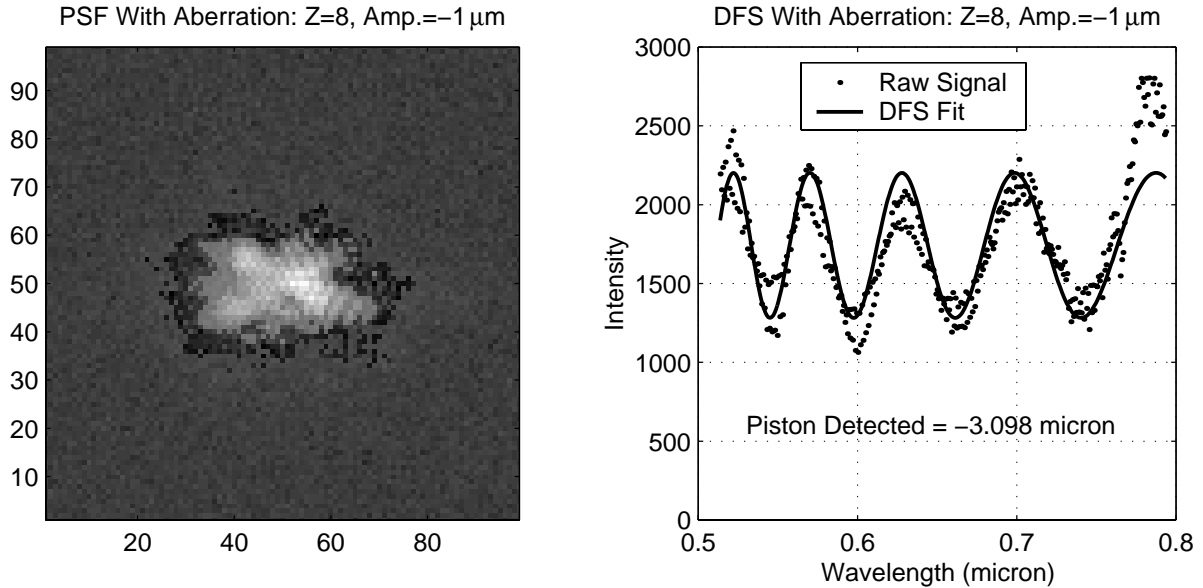


Figure 6. WCT experiment on the effect of segmented mirror surface aberrations. *Left:* PSF after the segments have been realigned, shown on a logarithmic scale. *Right:* the raw DFS signal and the DFS piston detection fit to the data.

For the segmented mirror radius mismatch the simulation using the optical model of WCT has shown that DFS can tolerate up to 0.25% of radius mismatch for visible light. Future updates of the WCT will provide the capability to validate the predicted effect of segment radius mismatch on DFS performance.

Another potential source of error is line-of-sight jitter and inter-segment jitter. The former is an ensemble of wavefront tilts, which results in an overall smear of the DFS fringe, and the latter causes wavefront tilts within each segment and results in the degradation of the co-centering of the segments in which the DFS fringe is formed. Both types of the jitter will lower the DFS visibility and fringe signal intensity, and therefore, lower the DFS signal-to-noise ratio. Detailed simulations have been performed to study the effect of jitter on DFS performance and DFS has shown to have large tolerance for the jitters. Experiments to study these effects will follow soon.

4. CONCLUSIONS AND FUTURE WORK

Modeling and experiments on NGST's Wavefront Control Testbed have shown that the dispersed fringe sensor is an effective and accurate method for detecting the piston errors between segmented mirrors. Coarse phasing with the DFS is a critical step in the NGST wavefront sensing and control process. The DFS has a dynamic range capable of detecting piston as large as one or more depths-of-focus and an accuracy of a fraction of a wavelength. This high dynamic range and good accuracy enables the DFS to correct piston errors that are too small for coarse alignment, but too large for the fine phasing process. Because the DFS piston detection algorithm uses a least squares fit to the DFS fringe to solve a few parameters that govern the fringe equation, the algorithm has a high tolerance for unfavorable effects such as jitter, segment misalignment, and mirror figure aberrations, therefore making the DFS a robust coarse phasing algorithm. Compared with other phasing techniques^[9], the DFS is very effective. One DFS fringe image normally provides enough information to phase one segmented mirror. Sub-grouping the segments enables multiple fringes in one image which can further reduce the number of images needed and increase the efficiency of the coarse phasing process.

The DFS algorithm was developed using realistic models of the testbed. However, experiments have been critical in developing the DFS algorithm. Applying the DFS algorithm on the testbed helps to uncover problems that occur only when dealing with a real system. The experiments on the WCT testbed have validated many results from the modeling. Aside from the environmental uncertainties such as lab seeing and testbed drift, the experimental results agree with the predictions of the models. Model validation enables us to continue to use the optical models to explore system performance, guiding our system design and predicting system performance. As the testbed evolves closer to the real NGST system, the DFS algorithm will also evolve to suit the needs of the system.

Although segment coarse phasing with a DFS is a powerful and efficient method, the algorithm has some limitations. First, the DFS can only sense the relative wavefront piston between segmented mirrors. The DFS cannot sense the relative tilt between the segments, nor can it sense any other low-order wavefront aberrations. However, residual segment tilts can be effectively sensed and corrected by either coarse alignment which uses the image differentiation centroid, or more accurately, by the In-focus PSF Optimizer^[7] and by the fine phasing which uses phase retrieval. Second, the accuracy of the DFS is still very coarse and requires fine phasing to further bring down the wavefront error. Third, the DFS fringe contrast depends on the relative orientation between the DFS dispersion and segment baseline as well as on the sparseness of the aperture. For a system with many segments, two grisms with perpendicular dispersion orientations may be needed to provide high-contrast fringes for all the possible segment pairing combinations.

The experiments have shown that an important factor in DFS detection accuracy is the fringe sampling. PSF under-sampling will have an adverse effect on the DFS performance. The PSF sampling issue has appeared in many forms in our modeling and experiments, such as the aperture sparseness and fringe visibility changes against the rotation of grism. This issue will require further study.

Experimental activities on WCT are still ongoing. The WCT is also evolving, adding complexity and approaching higher technology readiness levels by using more flight hardware. These testbed updates and modifications will provide more test metrics to validate the models^[4]. They will provide rich testing environments and challenges so the DFS algorithm as well as the testbed STCS can be thoroughly tested out before the launch of NGST.

5. ACKNOWLEDGEMENTS

The work reported here is the result of efforts from all the members in the NGST wavefront sensing and control team both at Jet Propulsion Laboratory and Goddard Space Flight Center. This work was performed at the Jet Propulsion Laboratory, California Institute of Technology, under contract with the National Aeronautics and Space Administration.

6. REFERENCES

- [1] D. Redding, S. Basinger, C. Bowers, R. Burg, L. Burns, D. Cohen, B. Dean, J. Green, A. Lowman, C. Ohara, and F. Shi, "Next Generation Space Telescope wavefront sensing and control," SPIE paper **4850**-49, Waikoloa, Hawaii (2002).
- [2] D. Redding, S. Basinger, C. Bowers, L. Burns, D. Cohen, B. Dean, P. Dumont, J. Green, A. Lowman, C. Ohara, and F. Shi, "Image-based wavefront sensing and control experiment," SPIE paper **4850**-62, Waikoloa, Hawaii (2002).
- [3] F. Shi, D. Redding, C. Bowers, A. Lowman, S. Basinger, T. Norton, P. Petrone, P. Davila, M. Wilson, and R. Boucarut, "DCATT dispersed fringe sensor: modeling and experimenting with the transmissive phase plates," Proc. SPIE **4013**, 757 – 762, Munich, Germany (2000).
- [4] P. Petrone, S. Basinger, C. Bowers, D. Cohen, L. Burns, A. Chu, P. Davila, P. Dogota, B. Dean, J. Green, K. Ha, W. Hayden, D. Lindler, A. Lowman, C. Ohara, D. Redding, F. Shi, M. Wilson, and B. Zukowski, "Optical design and performance of the NGST wavefront control testbed," SPIE paper **4850**-55, Waikoloa, Hawaii (2002).
- [5] S. Basinger, D. Redding, F. Shi, D. Cohen, J. Green, C. Ohara, A. Lowman, L. Burns, "Wavefront sensing and control software for a segmented space telescope," SPIE paper 4850-56, Waikoloa, Hawaii (2002).
- [6] A. Lowman, F. Shi, D. Redding, S. Basinger, C. Bowers, and P. Davila, "Telescope simulator for the DCATT testbed," Proc. SPIE **4013**, 954 – 961, Munich, Germany (2000).
- [7] C. Ohara, D. Redding, F. Shi, and J. Green, "PSF monitoring and in-focus wavefront control for NGST," SPIE paper **4850**-64, Waikoloa, Hawaii (2002).
- [8] "NanoPosition 1998," Physik Instrumente Catalog, 1998.
- [9] F. Shi, D. Redding, A. Lowman, C. Ohara, L. Burns, P. Petrone, C. Bowers, and S. Basinger, "Segmented mirror coarse phasing with white light interferometry: modeling and experiment on NGST's Wavefront Control Testbed," SPIE paper **4850**-59, Waikoloa, Hawaii (2002).
- [10] NGST's WCT web site: <http://www.ngst.nasa.gov/Hardware/text/WCT.html>
- [11] L. Burns, S. Basinger, T. Beck, J. Deering, D. Tonnu, D. Lindler, A. Lowman, R. Morris, C. Ohara, P. Petrone, D. Redding, J. Schott, S. Stoner, and L. Wheeler, "Wavefront Control Testbed integrated software system," SPIE paper **4850**-58, Waikoloa, Hawaii (2002).